pubs.acs.org/Biomac

Article

Impact of Polyethylene Glycol (PEG) Conformations on the *In Vivo* Fate and Drug Release Behavior of PEGylated Core-Cross-Linked Polymeric Nanoparticles

Takuma Kanamaru, Kazuo Sakurai, and Shota Fujii*

Cite This: *Biomacromolecules* 2022, 23, 3909−3918

Read Online

ACCESS | Metrics & More | Article Recommendations | Supporting Information

ABSTRACT: In cancer chemotherapy, core-cross-linked particles (CCPs) are a promising drug carrier due to their high structural stability in an *in vivo* environment, resulting in improved tumor delivery. A biocompatible polymer of polyethylene glycol (PEG) is often utilized to coat the surface of CCPs to avoid nonspecific adsorption of proteins *in vivo*. The PEG density and conformation on the particle surface are important structural factors that determine the *in vivo* fate of such PEGylated nanoparticles, including their pharmacokinetics and pharmacodynamics. However, contrary to expectations, we found no significant differences in the *in vivo* pharmacokinetics and pharmacodynamics of the PEGylated CCPs with the different PEG densities including mushroom, brush, and dense brush conformations. On the contrary, the *in vivo* release kinetics of hydrophilic and hydrophobic model drugs from the PEGylated CCPs was strongly dependent on the PEG conformation and the drug polarity. This may be related to the water-swelling degree in the particle PEG layer, which promotes and inhibits the diffusion of hydrophilic and hydrophobic drugs, respectively, from the particle core to the water phase. Our results provide guidelines for the design of cancer-targeting nanomedicine based on PEGylated CCPs.

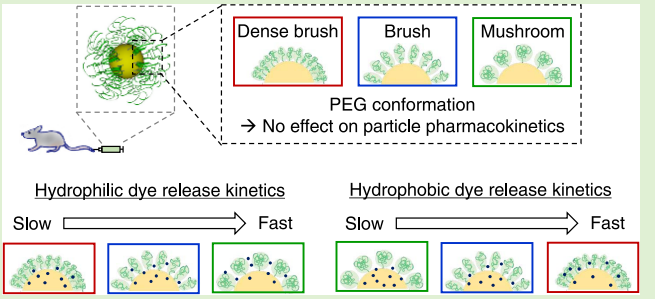

1. INTRODUCTION

The development of nanoparticles that can improve the low water solubility and limited pharmacokinetics (PK) of hydrophobic anticancer drugs has been the subject of cancer chemotherapy research for decades.[1−6] In particular, the utilization of polymeric micelles, which comprise a hydrophobic core to encapsulate hydrophobic drugs and a shell with hydrophilic polymer chains, for drug delivery has been the subject of intensive study since its initial proposal several decades ago.[7−12] For polymeric nanoparticles to accumulate at a target tumor site, they must evade clearance by the reticuloendothelial system (RES) and circulate stably in the bloodstream after administration.[13] This can be achieved by coating the nanoparticles with biocompatible polymers to inhibit nonspecific protein adsorption, which has become a universally accepted technology for the design of nanomedicines.[14−18] Polyethylene glycol (PEG) is a representative biocompatible polymer that has been introduced into nanomedicines to improve their pharmacokinetics.[19−22] In addition to polymeric micelles, PEG is also utilized to improve the biocompatibility of many types of nanomedicines, including proteins,[23] polymer systems,[24,25] metal nanoparticles,[20,26−28] and lipid nanoparticles,[29,30] such as for the recently developed coronavirus disease 2019 (COVID-19) vaccines.

However, the conjugation of PEG (i.e., PEGylation) to polymeric micelles is insufficient to achieve the desired *in vivo* PK and pharmacodynamics (PD) for improved anticancer efficacy. Shen et al.[31] reported that a large amount (∼80%) of PEGylated polymeric micelles composed of PEG-*b*-poly(ε-caprolactone) and PEG-*b*-poly(D,L-lactide) (PLA) dissociated into unimers immediately after injection into the bloodstream, which they attributed to shear stress in blood vessels and protein interactions. This dissociation also occurred in the case of a polymeric micelle with a polystyrene (PS) block, which has a high glass transition temperature (T_g) of 107 °C relative to body temperature, and the degree of dissociation depended on the molecular weight of the hydrophobic polymer. A method to solve micellar structural instability is to perform cross-linking reactions in the micellar core to produce core-cross-linked particles (CCPs). CCPs are no longer micelles because they are not in dynamic equilibrium and exhibit high structural stability even in an *in vivo* environment, which results in prolonged blood circulation and improved tumor delivery.[32] A previous study reported a method for preparing CCPs via the formation of nanoemulsions composed of cross-linkable

Received: June 9, 2022
Revised: July 29, 2022
Published: August 9, 2022

https://doi.org/10.1021/acs.biomac.2c00730
Biomacromolecules 2022, 23, 3909−3918

silicone-based oil molecules stabilized by PEGylated surfactants.[33] The CCPs exhibited very high stability even in an *in vivo* environment, resulting in longer blood circulation than that of PEGylated micelles.

Other structural factors that must be considered in controlling the *in vivo* PK and PD of PEGylated nanoparticles are the PEG density and conformation on the nanoparticle surface.[34−37] Cao et al.[38] controlled the PEG conformation on micelles comprising PEG-*b*-PLA by changing the molecular weight of the PLA block. They reported that the PEG conformation and density on the PEG-*b*-PLA micelle is a major structural factor that determines the protein binding affinity to the micelle, which has a dominant effect on the *in vivo* behavior of the micelles, including the PK and Kupffer cell uptake. Because of the difference in structural stability between CCPs (which are in nondynamic equilibrium) and polymeric micelles (which are in dynamic equilibrium), CCPs may exhibit a different PEG chain density dependence on the *in vivo* PK and PD from micellar systems.

In this study, we prepared PEGylated CCPs composed of a silicone-based core via an emulsion-mediated process and precisely characterized the particle structure using small-angle light and X-ray scattering techniques to elucidate the PEG conformation on the nanoparticles. We then investigated the impact of the PEG conformation of the PEGylated CCPs on their *in vivo* PK and PD. We also evaluated the effect of the PEG conformation on the *in vivo* release kinetics of the model drugs contained in the PEGylated CCPs. This study clarifies the importance of PEG conformation and contributes to the design of PEGylated CCPs.

2. MATERIALS AND METHODS

2.1. Materials. 3,5-Dihydroxybenzaldehyde, undecyl, propargyl bromide, sodium azide, methoxypolyethyelene glycol azide (number-average molecular weight (M_n) = 1 and 2 kDa), methoxypolyethyelene glycol alkyne (M_n = 5 kDa), and platinum(0)-1,3-divinyl-1,1,3,3-tetramethyldisiloxane complex solution (denoted Karstedt's catalyst solution) were purchased from Sigma-Aldrich and used as received without further purification. Cy5 alkyne, sulfonated Cy5 azide, and Cy5 azide were purchased from Lumiprobe. Other reagents and solvents were purchased from TCI. All reactions were performed under a nitrogen atmosphere. Nuclear magnetic resonance (NMR) spectra were recorded with a 500 MHz JEOL spectrometer using chloroform-*d* as the solvent. Details of the synthesis and preparation procedure of the PEGylated surfactants and CCPs are provided in the Supporting Information.

2.2. Dynamic Light Scattering (DLS) Measurements. The hydrodynamic diameters of PEGylated micelles and CCPs in 150 mM aqueous NaCl or 80% methanol aqueous solution were evaluated by DLS measurements using a Beckman Coulter DelsaMax instrument at 25 °C and a scattering angle of 163.5°.

2.3. Dry and Cryogenic Transmission Electron Microscopy (Dry and Cryo-TEM). TEM observations were performed using a JEOL JEM-2100Plus electron microscope operated at an accelerating voltage of 200 kV. For dry-TEM, 10 μL of CCP solution (2.5 mg mL^{-1} in 150 mM aqueous NaCl) was placed on a TEM grid coated with elastic carbon film. After 10 min, the sample solution was swabbed with filter paper and then immediately stained by mounting a droplet of Nano-W (Nanoprobes, aq. 2% w/v) on the grid for 1 s and swabbed quickly. The grid was dried under vacuum and then loaded into the JEOL JEM-2100Plus electron microscope. For cryo-TEM, samples were prepared on plasma-treated QUANTIFOIL holey carbon grids (R2/1). Then, 3 μL of CCP solution (10 mg mL^{-1} in 150 mM aqueous NaCl) was blotted using a Leica EM GP2 plunge freezer and was then immediately plunged and frozen in liquid ethane. The prepared samples were transferred to the microscope instrument by utilizing a Gatan transfer stage.

2.4. Small-Angle X-ray Scattering (SAXS) Measurements. SAXS measurements were performed at the BL-40B2 beamline of the SPring-8 facility in Hyōgo, Japan. The wavelength of the incident light (λ) and the camera distance were adjusted to 0.10 nm and 2 m, respectively. These setup conditions provided a q range of 0.080−3.0 nm^{-1}, where q is the magnitude of the scattering vector and is defined as $q = 4\pi \sin\theta/\lambda$ with a scattering angle of 2θ. Scattering patterns were collected for 180 s using a Dectris Pilatus-3S 2M detector. Measurements were performed for the diluted solution of PEGylated micelles and CCPs in 150 mM aqueous NaCl at 2.5 mg mL^{-1}, which was a sufficiently low concentration to ignore interparticle interactions.

The following core−shell spherical model was employed to analyze PEGylated micelles

$$I(q)_{\mathrm{cs-sphere}} = \left\{3V_c\Delta\rho_c\frac{j_1(qR_c)}{qR_c} + 3V_s\Delta\rho_s\frac{j_1(qR_s)}{qR_s}\right\}^2 \quad (1)$$

where R_c and R_s are the radii of the core and whole particle, respectively; $\Delta\rho_c$ (=$\rho_c-\rho_s$) and $\Delta\rho_s$ (=$\rho_s-\rho_{sol}$) are the electron density contrasts of the core and shell, respectively, where ρ_c, ρ_s, and ρ_{sol} are the electron densities of the core, shell, and surrounding solvent, respectively; j_1 is the second spherical Bessel function; and V_c and V_s are the volumes of the core and whole particle, respectively. For PEGylated CCPs, the core−shell spherical model was modified by the addition of the Ornstein−Zernike (OZ) equation, which considers scattering from the cross-linked structure as independent when the mesh size (ξ) is sufficiently small relative to the particle size.[39] The modified model is described as follows[33]

$$I(q)_{\mathrm{cs-sphere-OZ}} = \left\{3V_c\Delta\rho_c\frac{j_1(qR_c)}{qR_c} + 3V_s\Delta\rho_s\frac{j_1(qR_s)}{qR_s}\right\}^2 + \frac{I_{OZ}(0)}{1+q^2\xi^2} \quad (2)$$

where $I_{OZ}(0)$ is a constant value. For the SAXS profile of PEGylated CCPs with longer PEG chains (average M_n = 5 kDa), a spherical model with Gaussian corona chains attached to the core surface was employed as follows[44]

$$I_{\mathrm{sphere-GC-OZ}}(q) = \left[\Delta\rho_c V_c\frac{j_1(qR_c)}{qR_c} + \Delta\rho_s V_s S_{ss}(q)\right]^2 + \frac{\{\Delta\rho_s V_s\}^2}{N}(F_s(q) - S_{ss}(q)) + \frac{I_{OZ}(0)}{1+q^2\xi^2} \quad (3)$$

where N is the number of corona chains. $F_s(q)$ and $S_{ss}(q)$ are the self-correlation terms of the spherical core and Gaussian chain, respectively, and represent the interference between the chains in the corona shell

$$S_{cc}(q) = \frac{1-\exp(-q^2R_g^2)}{q^2R_g^2}\left[\frac{\sin(q(R_c+R_g))}{q(R_c+R_g)}\right]^2 \quad (4)$$

$$F_c(q) = \frac{2[\exp(-q^2R_g^2) - 1 + q^2R_g^2]}{(q^2R_g^2)^2} \quad (5)$$

where R_g is the radius of gyration of a Gaussian chain.

2.5. Asymmetrical Flow Field-Flow Fractionation (AF4) Measurements. The sample solutions (2.5 mg mL^{-1}) were injected into an AF4 module (Eclipse AF4, Wyatt Technology, Santa Barbara, CA) equipped with a 10 kDa regenerated cellulose membrane at 25 °C. The fractionated output was then passed sequentially through a UV detector, a Dawn Heleos II multiangle light scattering (MALS) detector (Wyatt Technology), and an Optilab rEX DSP differential

https://doi.org/10.1021/acs.biomac.2c00730
Biomacromolecules 2022, 23, 3909−3918

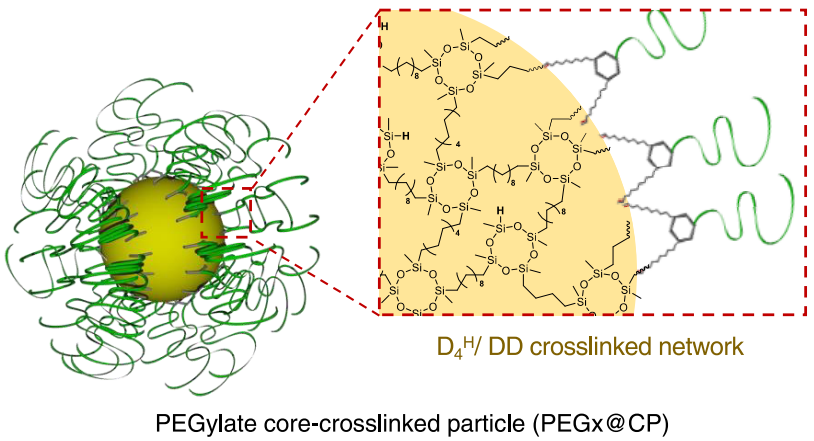

Figure 1. Schematic illustration of a PEGylated core-cross-linked particle (**PEGx@CP**) comprising a D_4^H/DD cross-linked network core.

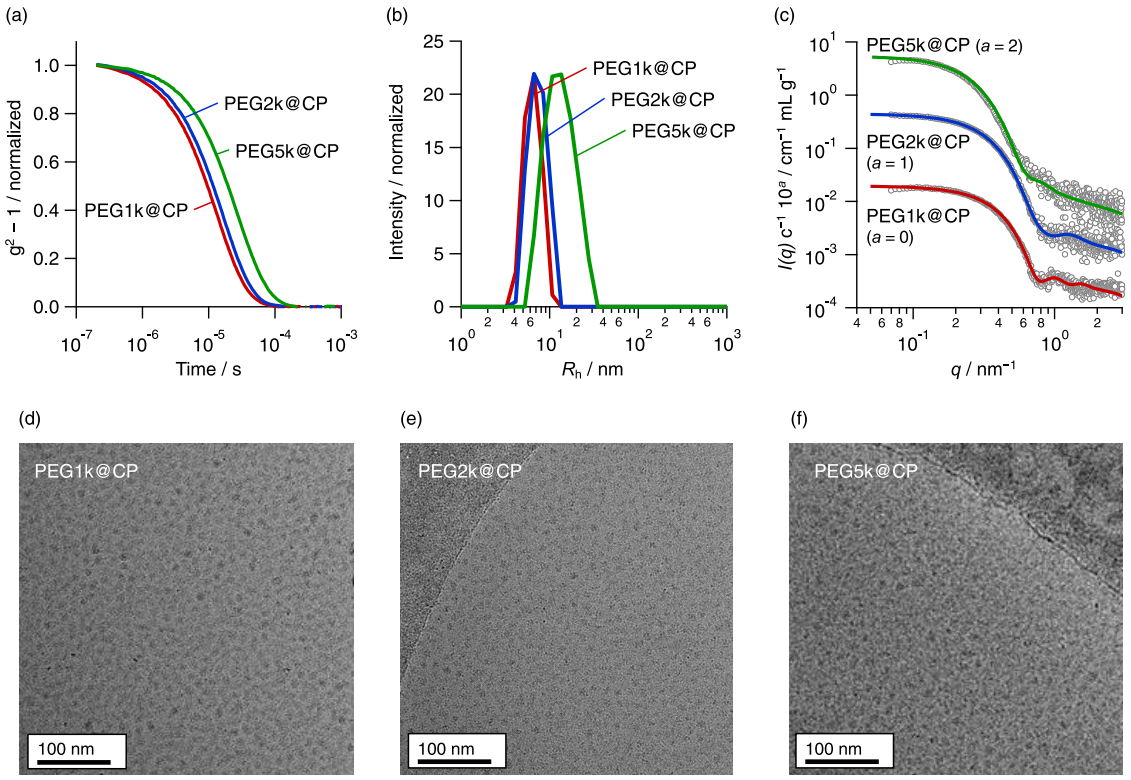

Figure 2. (a) Dynamic light scattering (DLS) autocorrelation function and (b) DLS histogram of **PEGx@CPs** in 150 mM aqueous NaCl (red, **PEG1k@CP**; blue, **PEG2k@CP**; green, **PEG5k@CP**). (c) Small-angle X-ray scattering profile of **PEGx@CPs** in 150 mM aqueous NaCl. Gray circles represent the experimental data, while colored solid lines represent the theoretical profiles calculated using a core−shell spherical model with the Ornstein−Zernike (OZ) function for **PEG1k@CP** (red) and **PEG2k@CP** (blue) or a sphere with attached Gaussian chains and the OZ function for **PEG5k@CP** (green). Cryogenic transmission electron microscopy images of (d) **PEG1k@CP**, (e) **PEG2k@CP**, and (f) **PEG5k@CP** in 150 mM aqueous NaCl.

refractive index (RI) detector (Wyatt Technology) operating at a wavelength of 658 nm. The cross flow was exponentially reduced over the measurement time. The specific RI increment ($\partial n/\partial c$) and extinction coefficient (ε at 280 nm) of the samples in 150 mM NaCl aqueous solution were determined using a DRM-1021 differential refractometer (Otsuka Electronics, Osaka, Japan) and a Jasco V-630 UV−vis spectrometer (Tokyo, Japan), respectively (see Figure S1).

2.6. Animal Experiments. All animal experiments were conducted in accordance with the Guiding Principles for the Care and Use of Laboratory Animals of the University of Kitakyushu. BALB/c mice (male, 6 weeks old) were purchased from Japan SLC Co. (Shizuoka, Japan).

2.7. *In Vivo* PK and Biodistribution. Mouse CT26 colon cancer cells suspended in Hank's balanced saline solution (HBSS) buffer at a concentration of 10^7 cells mL^{-1}, and 0.1 mL of the solution was implanted into the right back of the mice. When the tumor volumes were confirmed to be approximately 300 mm^3, 100 μL of either PEGylated micelles containing nitrobenzoxadiazole-labeled lipids, Cy5-labeled PEGylated CCPs, or PEGylated CCPs containing Cy5 derivatives was administered intravenously into the tumor-bearing mice via the tail vein. All doses of these samples were fixed as 1.0 quadrillion nanoparticles to eliminate the effect of dosage on the sample PK and PD. Blood samples (20 μL) were collected from the tail at various times. The collected blood samples were centrifuged at 1200*g* for 15 min at 4 °C to obtain serum sample solutions. The

https://doi.org/10.1021/acs.biomac.2c00730
Biomacromolecules 2022, 23, 3909−3918

fluorescence intensity of the collected samples was measured using a Pharos FXTM Plus Molecular Imager (Bio-Rad Laboratories). For the calculation of the initial sample concentration in the blood of the mice, we assumed that the total blood volume was 7% of their body weight.[40] Twenty-four hour after injection, blood samples were taken from the posterior vena cava of the anesthetized mice. After transcardial perfusion with phosphate-buffered saline (PBS), organs including the heart, lung, liver, kidney, and spleen were collected along with tumor tissues. After the organs and tissues were weighed, 1.0 mL of PBS was added, and the mixture was homogenized using a gentleMACS Dissociator (Miltenyi Biotec GmbH) with the standard C Tubes program. The solution and tissue fragments were separated by centrifugation at 12,000*g* for 15 min at 4 °C. The fluorescence of the supernatants was measured using a Pharos FXTM Plus Molecular Imager (Bio-Rad).

3. RESULTS AND DISCUSSION

3.1. Preparation of PEGylated CCPs. We synthesized PEGylated surfactants with diundecyl chains called **P$_x$DU**, where **x** represents the PEG molecular weight, by following the procedure in a previous report.[33] The synthesis procedure is presented in Scheme S1 and is described in detail in the Supporting Information. Briefly, we introduced undecyl chains into the phenolic hydroxyl groups of 3,5-dihydroxybenzaldehyde by the Williamson ether reaction. Aldehyde was reduced to alcohol with sodium borohydride, and a propargyl group was attached by the Williamson ether reaction. Finally, an azide group at the end of the PEG chain (M_n = 1 or 2 kDa) was reacted with the propargyl group by azide−alkyne click chemistry to produce the PEGylated surfactants **P$_{1k}$DU** and **P$_{2k}$DU**. For **P$_{5k}$DU**, we synthesized an azide with an attached hydrophobic moiety and then introduced PEG (M_n = 5 kDa) with an alkyne group at the end of the chain via click chemistry. The chemical structures of the final products **P$_{1k}$DU**, **P$_{2k}$DU**, and **P$_{5k}$DU** were confirmed by ^{1}H NMR (Figures S2−S4). The molecular weights of **P$_{1k}$DU**, **P$_{2k}$DU**, and **P$_{5k}$DU** were confirmed to be 1.6, 2.5, and 5.5 kDa, respectively, by matrix-assisted laser desorption/ionization time-of-flight (MALDI-TOF) mass spectrometry (Figures S5−S7). These weights were similar to the molecular weights calculated from the chemical structures.

CCPs via nanoemulsion were prepared by following the procedure in our previous report.[33] As illustrated in Figure S8, we first prepared a **P$_x$DU** micellar solution containing Karstedt's catalyst in 150 mM aqueous NaCl. Cross-linking agents including 1,3,5,7-tetramethylcyclotetrasiloxane (D_4^H) containing four silyl groups and decadiene (DD) dissolved in dioxane were added to the micellar solution and then vigorously mixed with a probe-type ultrasonic homogenizer for 1 min. This procedure produced nanoemulsions comprising the oil phase of the cross-linkers covered with **P$_x$DU**. Simultaneously, the nanoemulsion structure was captured by the formation of a cross-linking structure through the hydrosilylation reaction[41] between the silyl group of D_4^H and the vinyl group of DD in the oil phase. The vinyl group of **P$_x$DU** was also involved in the formation of the cross-linking structure. Finally, the solution was heated at 60 °C for 20 min to end the reaction and purified by spin dialysis three times with 150 mM aqueous NaCl. Hereafter, CCPs bearing PEG are denoted **PEGx@CP**, where **x** indicates the PEG molecular weight (Figure 1).

3.2. Structural Characterization of PEGylated CCPs. Figure 2a,b presents the autocorrelation function and DLS histogram, respectively, of the **PEGx@CP**s in 150 mM aqueous NaCl. The relaxation time in the DLS autocorrelation function increased with the PEG molecular weight, which indicates an increase in the particle size. The hydrodynamic radii (R_h) of **PEG1k@CP**, **PEG2k@CP**, and **PEG5k@CP** were determined from the DLS data as 6.5, 7.5, and 13.8 nm, respectively, and are summarized in Table 1. The DLS results indicate that the R_h values of the **P$_{1k}$DU**, **P$_{2k}$DU**, and **P$_{5k}$DU** micelles were 4.6, 6.1, and 8.9 nm, respectively (Figure S9), also exhibiting dependence on the PEG molecular weight. The particle size of the **PEGx@CP**s was approximately 1.2−1.5 times that of the precursor micelles, which can be attributed to the formation of an intermediate nanoemulsion, whose particle size should be larger than that of the original micelles, to form the core-cross-linked structure. The particle size of the **PEGx@CP**s did not change in a good solvent (80 vol% of methanol aqueous solution) for **P$_x$DU**s, whereas the **P$_x$DU** micellar size changed significantly (Figure S10). This indicates that the structural stability of **PEGx@CP**s can be attributed to the core-cross-linked structure.

Table 1. Particle Characteristics of PEGx@CPs and Speculated PEG Conformations

sample name	R_h[a] [nm]	R_c[b] [nm]	M_w[c] [10^5 g mol^{-1}]	number of PEG chains[d]	PEG conformation[e]
PEG1k@CP	6.5	1.5	3.03	194	dense brush
PEG2k@CP	7.5	2.0	3.00	110	brush
PEG5k@CP	13.8	6.2	3.86	65	mushroom

[a]Hydrodynamic radius determined by DLS measurements. [b]Core radius estimated by SAXS analysis. [c]Molar mass of the nanoparticles. [d]PEG chain number determined by AF4-MALS measurements. [e]PEG conformation estimated from structural characterization.

We performed SAXS measurements to characterize the internal particle structures of **P$_x$DU** micelles and **PEGx@CP**s. The SAXS profiles of the **PEGx@CP**s displayed clear Guinier regions following $I(q) \propto q^0$ in the low-q region, which indicated no secondary aggregation in the solution (Figure 2c).[42] As illustrated in Figure S11, the Guinier regions in the SAXS profiles of **P$_x$DU** micelles were similar to those of **PEGx@CP**s. The SAXS profiles of all **P$_x$DU** micelles could be reproduced using a simple core−shell spherical model, where the core and shell comprised the hydrophobic moiety and PEG in **P$_x$DU**, respectively. However, the fitting model could not reproduce the SAXS profiles of **PEGx@CP**s because they differed in the high-q region from the scattering profiles of the micelles. As previously reported,[33,43] a cross-linked structure in the particle core causes independent scattering described by the OZ function comprising the correlation length (ξ) corresponding to the mesh size. Thus, the scattering profile in the high-q region of the **PEGx@CP**s was flat relative to that of the micelles, especially for **PEG1k@CP** and **PEG2k@CP**. In the case of **PEG5k@CP**, the scattering intensity in the high-q region followed $I(q) \propto q^{-2}$, which indicates that the scattering factor attributed to the Gaussian chain of PEG overwhelmed that from the core structure.[44] These differences in the SAXS profiles of the **PEGx@CP**s suggest different PEG conformations on the particle shell.

For **PEG1k@CP** and **PEG2k@CP**, the core−shell spherical model with the OZ function could reproduce their SAXS profiles, while the SAXS profile of **PEG5k@CP** could be reproduced using a spherical model with attached Gaussian chains and the OZ function. The fitting parameters are

https://doi.org/10.1021/acs.biomac.2c00730
Biomacromolecules 2022, 23, 3909−3918

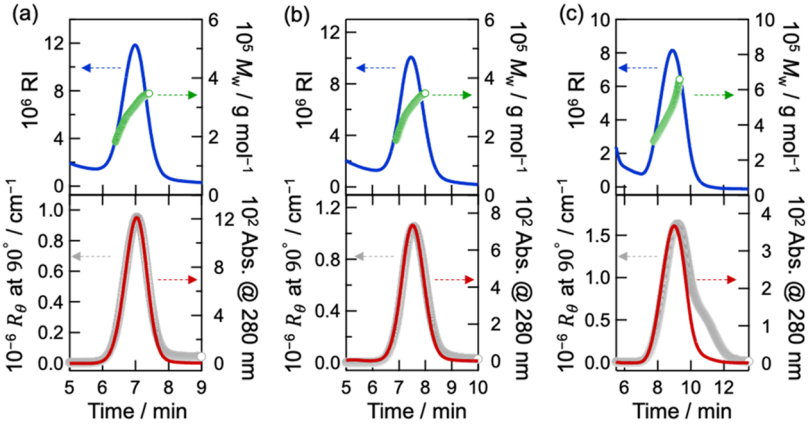

Figure 3. Asymmetrical flow field-flow fractionation (AF4) fractograms of (a) **PEG1k@CP**, (b) **PEG2k@CP**, and (c) **PEG5k@CP** eluted with 150 mM aqueous NaCl and measured by LS (gray circles), UV (red line), and refractive index (RI) (blue line) detectors. The green points represent the particle molar mass determined at each fraction.

summarized in Table S1. The electron densities of the particle core and shell were estimated to be 342 and 337 e nm^{-3}, respectively, which are similar to those of a similar CCP system.[33] We also confirmed that the scattering profiles of **PEG1k@CP** and **PEG2k@CP** at 25 and 37 °C were comparable, which indicates that the particle structure is insensitive to temperature within this range. In addition, we confirmed their particle morphology through cryo- and dry-TEM, as illustrated in Figures 2d and S12. All **PEGx@CP**s were observed as spherical objects, which was consistent with the SAXS analysis. The particle sizes of **PEG1k@CP** and **PEG2k@CP** as estimated from their cryo-TEM images mostly corresponded to those determined by the DLS measurements, whereas the particle size of **PEG5k@CP** was slightly smaller than that estimated by DLS measurements. In contrast, the particle size of **PEG5k@CP** as estimated by conventional dry-TEM was mostly consistent with the DLS results. Based on the SAXS analysis, PEG in the shell of **PEG5k@CP** could be inferred as having a highly motile Gaussian chain conformation, which allowed the solvent to infiltrate the PEG moiety more than for the other **PEGx@CP**s. Thus, the electron density contrast between the shell and solvent was very small, which may have made it difficult to observe the whole particle structure with cryo-TEM, especially for **PEG5k@CP**.

To determine the number of PEG chains on **PEGx@CP**s, we performed MALS measurements on a fractionated sample using the AF4 system. Figure 3 summarizes the AF4 fractograms of **PEGx@CP**s detected by the RI, UV, and MALS detectors. We also performed AF4-MALS measurements for **P$_x$DU** micelles, which are summarized in Figure S13. The RI profiles detecting the particle concentration were unimodal for all particle systems and almost overlapped with their LS profiles, which indicates monodispersity. For **PEG5k@CP**, the LS profile had a shoulder at approximately 11 min, which may have been caused by the presence of an aggregate in the sample solution. However, the effect of the aggregate on the particle properties was negligible because the concentration of the aggregate was very low (<1 wt %), as indicated in the RI profile.

The weight-average molar mass (M_w) was determined for all particles, and the values are summarized in Tables 1 and S2. The M_w of **PEGx@CP**s ($M_{w,PEGx@CP}$) is given by[33]

$$M_{w,PEGx@CP} = M_{w,cross-linker} \times N_{agg,cross-linker} + M_{w,PxDU} \times N_{agg,PxDU} \quad (6)$$

where $M_{w,cross-linker}$ and $M_{w,PxDU}$ are the average molecular weights of the cross-linking agents and **P$_x$DU**s, respectively. $N_{agg,cross-linker}$ and $N_{agg,PxDU}$ are the number of cross-linker molecules and **P$_x$DU**s, respectively, in the **PEGx@CP**s. The UV absorbance at 280 nm detected in the AF4 fractogram was used to determine the **P$_x$DU** concentration in the **PEGx@CP**s because of the benzene group in the chemical structure, while the whole particle concentration was determined from the RI signal. Based on these data, the molar ratio of the cross-linker to **P$_x$DU** ([cross-linker]/[**P$_x$DU**]) was determined for each fraction. By substituting $N_{agg,PxDU} \times$ [cross-linker]/[**P$_x$DU**] into the term $N_{agg,cross-linker}$ in eq 6 and solving for $N_{agg,PxDU}$, we determined the number of PEG chains on each particle. The numbers of PEG chains in **PEG1k@CP**, **PEG2k@CP**, and **PEG5k@CP** were 194, 110, and 65, respectively, as summarized in Table 1. The PEG chain number decreased as the PEG molecular weight increased in the **P$_x$DU**s. This may be because the structural characteristics of the **P$_x$DU** micelles, whose aggregation number (N_{agg}) followed the packing parameter theory,[45] affected the **PEGx@CP** structures. In fact, the N_{agg} values of the **P$_x$DU** micelles also decreased with the PEG molecular weight because a larger head volume reduces N_{agg} in micellar systems.

3.3. PEG Conformations on PEGx@CP Surfaces. Since PEG conformation on nanoparticles cannot be determined by PEG length but be speculated by PEG density, the structural characteristics of the **PEGx@CP**s were used to speculate the PEG conformations on the particle surfaces.[27,34,38] The PEG density at the particle core–shell interface (d_{PEG_cs}) and outermost surface of the particle–water interface (d_{PEG_pw}) was determined using the following equations

$$d_{PEG_{cs}} = \frac{N_{PEG}}{S_{cs}(=4\pi R_c^2)} \quad (7)$$

$$d_{PEG_{pw}} = \frac{N_{PEG}}{S_{pw}(=4\pi R_h^2)} \quad (8)$$

where R_h, R_c, and N_{PEG} denote the hydrodynamic radius determined by DLS measurements, the particle core radius estimated by SAXS analysis, and the number of PEG chains

https://doi.org/10.1021/acs.biomac.2c00730
Biomacromolecules 2022, 23, 3909–3918

determined by AF4-MALS measurements, respectively. The PEG density values are summarized in Table S3. The PEG density at both interfaces decreased with the PEG molecular weight, which indicated different PEG conformations for each particle. The physical parameters of the surface area of a single PEG chain (A), distance between PEG chains (D), PEG length in the particle shell (L), and Flory radius (R_F) (see Figure S14) were used to estimate the PEG chain conformations in the **PEGx@CPs**. These parameters were calculated as follows

$$A = \frac{S_{pw}}{N_{PEG}} \quad (9)$$

$$L = R_h - R_c \quad (10)$$

$$D = 2\sqrt{\frac{A}{\pi}} \quad (11)$$

$$R_F = 0.35n^{3/5} \quad (12)$$

where n is the number of monomer units in PEG.

The relationship between D and R_F was used to define the PEG conformations of the **PEGx@CPs**. **PEG5k@CP** had a mushroom conformation ($D/R_F > 1$), while **PEGx@1kCP** and **PEG2k@CP** had brush conformations ($D/R_F < 1$). Based on the relationship between R_F and L, **PEG1k@CP** had a dense brush conformation ($L/2R_F > 1$). Thus, we prepared three CCPs with different PEG conformations, as illustrated in Figure 4.

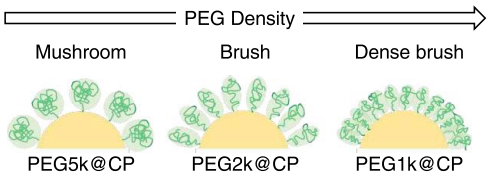

Figure 4. Schematic illustration of PEG conformations on **PEGx@CPs**: mushroom, brush, and dense brush.

3.4. *In Vivo* PK and PD of PEGx@CPs with Different PEG Conformations. To trace the *in vivo* PK and PD of **PEGx@CPs**, we prepared Cy5-labeled **PEGx@CPs** (**PEGx@CP^{Cy5}s**) by conjugating Cy5 alkyne and the silane group in D_4^H via hydrosilylation (DLS data of **PEGx@CP^{Cy5}s** are shown in Figure S15). Ouyang et al.[46] recently reported that the delivery efficiency of PEGylated nanoparticles to a tumor depends more on the dosage in terms of the number of particles than the size and targetability of the nanoparticles. They found that the kinetic dominance of nanoparticle uptake by Kupffer cells in the liver results in dose-dependent PK of PEGylated nanoparticles, and they observed no significant differences in the PK and tumor accumulation in the high-dose region (>10 trillion nanoparticles). To eliminate the effect of dosage, we fixed the injected dose (ID) of each particle to be 1.0 quadrillion nanoparticles, which is sufficiently large compared to the dose threshold. We also evaluated the blood kinetics of **P_{2k}DU** micelles containing 3.0 wt % nitrobenzoxadiazole (NBD)-labeled lipid (**$P_{2k}DU^{NBD}$**) as a fluorescence probe. For these micelles, the PEG conformation on the micelle surface was determined to be the brush conformation using the particle physical parameters evaluated above. Figure 5a presents the blood kinetics of **PEGx@CP^{Cy5}s** and **$P_{2k}DU^{NBD}$** after intravenous (IV) injection into BALB/c mice. As illustrated in Figure 5a, the micelles were rapidly cleared from the blood immediately after injection despite the brush PEG conformation, whereas all **PEGx@CP^{Cy5}s** remained at approximately 50% of the ID in the blood after 24 h. Interestingly, no significant differences were observed in the PK of **PEGx@CP^{Cy5}s** despite their different PEG conformations. Our results also demonstrate no significant differences in the accumulation level of the **PEGx@CP^{Cy5}s** in various organs and tumor tissues (Figure 5b).

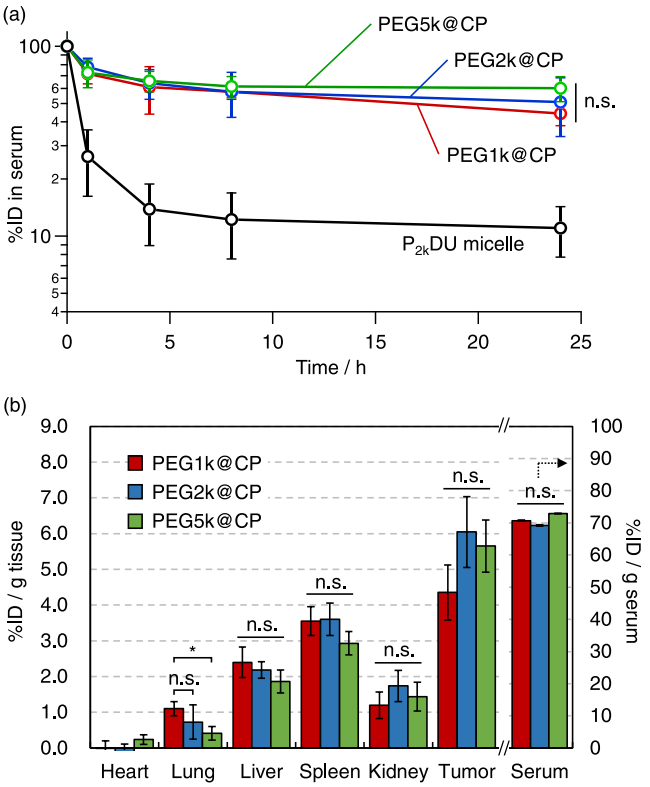

Figure 5. (a) *In vivo* pharmacokinetics of **PEGx@CP^{Cy5}s** (red, **PEG1k@CP^{Cy5}**; blue, **PEG2k@CP^{Cy5}**; green, **PEG5k@CP^{Cy5}**) and the **$P_{2k}DU^{NBD}$** micelle (black) after intravenous (IV) administration into mice at 1.0 quadrillion nanoparticles dosage. (b) Biodistribution of **PEGx@CP^{Cy5}s** (red, **PEG1k@CP^{Cy5}**; blue, **PEG2k@CP^{Cy5}**; green, **PEG5k@CP^{Cy5}**) 24 h after IV administration into mice. All data are represented as the mean ± standard deviation (n = 5). n.s., not significant. *P < 0.05 (one-way ANOVA with Tukey's multiple comparison test).

In PEGylated polymeric micellar systems, the PEG conformation in the particle shell has been reported to be an important structural factor in determining the *in vivo* PK and PD of the system.[34,38] However, no such PEG conformation dependence was observed for our PEGylated CCP system, as discussed above. The difference in the *in vivo* behavior between PEGylated micelles and CCPs indicates that the structural stability of the nanoparticles rather than PEG conformation is the critical structural factor determining the PK and PD. Micelles are inherently self-assembled particles via weak intermolecular interactions and are in dynamic equilibrium, resulting in easy dissociation in blood. Sun et al.[31] demonstrated that micellar dissociation in the blood is inevitable because the shear stress in the blood vessel induces dissociation of micelles containing PS as a hydrophobic block, which is known to be extremely stable owing to the glassy PS core.

https://doi.org/10.1021/acs.biomac.2c00730
Biomacromolecules 2022, 23, 3909−3918

As illustrated in Figure 5b, the accumulation in the liver of **PEGx@CP**^{Cy5}s 24 h after IV injection into mice was approximately 2% ID g^{-1}, which is much smaller than that of the $\mathbf{P_{2k}DU}^{NBD}$ micelles (~18% ID g^{-1}), as displayed in Figure S16. The relatively large amount of micellar accumulation in the liver also implies that the hydrophobic part of the surfactant was exposed to the water interface by dissociation of the micelles owing to the dynamic self-assembly system after IV injection. The hydrophobic moiety of the surfactant would have been subsequently opsonized by serum proteins, which promote recognition by liver Kupffer cells. In contrast, the cross-linked structure in the **PEGx@CP**s helped stabilize the particle structure and prevented the hydrophobic domain from being recognized by the RES, which prolonged the PK. In other words, the results suggest that PEGylated nanoparticles whose particle structure is not in dynamic equilibrium like micelles can escape rapid clearance from the blood as long as their hydrophobic core interface is somewhat covered with PEG chains.

3.5. *In Vivo* Release Kinetics of Hydrophobic and Hydrophilic Model Drugs from PEGx@CPs. We next investigated the effect of PEG conformation on the drug release kinetics *in vivo*. We prepared **PEGx@CP**s containing a sulfonated Cy5 derivative (sCy5) as a model hydrophilic drug, which was physically contained in the particle core, and intravenously injected the nanoparticle solution into mice at an ID of 1.0 quadrillion nanoparticles. As illustrated in Figure 6a, the blood retention of sCy5 contained in **PEG1k@CP** and **PEG2k@CP** with brush and dense brush PEG conformations, respectively, was significantly higher than that in **PEG5k@CP** with a mushroom PEG conformation. However, in the case of a more hydrophobic native Cy5 derivative (nCy5) without sulfonic acid groups, the PK exhibited the opposite order to that displayed in Figure 6a, with the highest amount of nCy5 in **PEG5k@CP** remaining in the blood 24 h after injection (Figure 6b).

We hypothesized that the difference in the release behavior of the sCy5 and nCy5 systems is related to the difference in polarity between the cross-linked core and the model drugs. The predicted octanol/water partition coefficients (P) of the cross-linkers comprising the cross-linked core and model drugs were calculated using the Molinspiration Property Calculation Service,[47] and their log values (miLog P) are summarized in Figure S17. The hydrophobic undecyl chain of $\mathbf{P_xDU}$ had a miLog P value of 6.17, which indicates hydrophobicity and is similar to the values for the crosslinkers decadiene (miLog $P_{decadiene}$ = 4.64) and D_H[4] (miLog P_{D4H} = 7.38). Because nCy5 (miLog P_{nCy5} = 5.39) was predicted to have a similar hydrophobicity to that of the particle core components, it was expected to mix homogeneously with them and become uniformly distributed in the particle core. Due to hydrophobicity, the released nCy5 should have a much higher accumulation level in organs/tissues than sCy5 (Figure S18). The miLog P value of sCy5 was −0.68, which indicates high hydrophilicity and a significant difference in polarity from the particle core components. Owing to its hydrophilicity, sCy5 cannot mix with the core components uniformly; therefore, it should be omnipresent near the hydrophilic PEG chains (miLog P_{PEG} = −0.52) at the particle core−shell interface.

According to the previous structural analysis, **PEG5k@CP** has a mushroom PEG conformation, which may allow water molecules to infiltrate the particle shell. Given that the molecular diffusion of the model drugs from the particle core

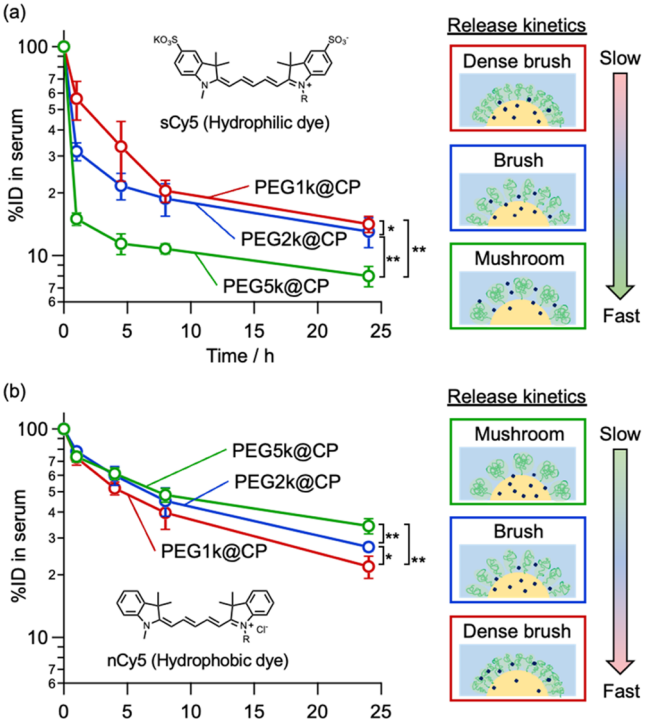

Figure 6. *In vivo* drug release kinetics of (a) sCy5 and (b) nCy5 included in **PEGx@CP**s (red, **PEG1k@CP**; blue, **PEG2k@CP**; green, **PEG5k@CP**) after intravenous administration into mice at a 1.0 quadrillion nanoparticles dosage. The chemical structures of sCy5 and nCy5 are displayed, where the R group is an alkyl chain with azide, and the details are displayed in Figure S17. All data are represented as the mean ± standard deviation (n = 5). n.s., not significant. *P < 0.05 and **P < 0.01 (one-way ANOVA with Tukey's multiple comparison test). The right images are schematic illustrations describing the relative release kinetics of each dye from **PEGx@CP**s with various PEG conformations.

to the water phase dominates the release kinetics, the release of the relatively hydrophilic sCy5 should be promoted in **PEG5k@CP**, whose shell is infiltrated most easily by water molecules. In the actual results, the elimination rate constant at the distribution phase (Ke_α) of sCy5 in the **PEGx@CP**s increased in order **PEG1k@CP** (Ke_α = 0.57 ± 0.24 h^{-1}), **PEG2k@CP** (Ke_α = 1.2 ± 0.1 h^{-1}), and **PEG5k@CP** (Ke_α = 1.9 ± 0.1 h^{-1}). Thus, the molecular diffusion of the contained dye dominated the overall release behavior, as illustrated in Figure 6a. For the relatively hydrophobic nCy5, diffusion from the core to the water-swollen PEG shell should be suppressed at the interface due to the hydrophobicity of nCy5. Based on this mechanism, the lowest PEG chain density in **PEG5k@CP** allowed the most water infiltration compared with other cases and thus inhibited the release of nCy5 more so than in other cases, as illustrated in Figure 6b. In the case of **PEG1k@CP**, nCy5 should easily diffuse from the core to the shell, presumably because of the lower infiltration of water molecules into the shell owing to the dense brush PEG conformation. This resulted in the relatively fast release profile of nCy5 compared with the other profiles.

Although nCy5 contained in the **PEGx@CP**s exhibited a relatively long retention time in blood, it accumulated more in various organs/tissues than sCy5 because of its hydrophobicity, as indicated in Figure S18. Furthermore, the accumulation level of **PEGx@CP**s (displayed in Figure 5b)

https://doi.org/10.1021/acs.biomac.2c00730
Biomacromolecules 2022, 23, 3909−3918

in various organs was much lower than that of nCy5 and sCy5. This indicates that to achieve drug delivery to the target tumor site without side effects induced by the undesirable accumulation of anticancer drugs in other healthy organs, one approach is to use chemical bonding to conjugate anticancer drugs to carrier nanoparticles that can be selectively cleaved at the target tumor site.[48,49] For this strategy to be effective, improving the structural stability of nanoparticles should be prioritized for the design of drug carriers.

4. CONCLUSIONS

We prepared PEGylated CCPs with different PEG conformations, which were precisely characterized using small-angle light and X-ray scattering techniques. The PK of the PEGylated CCPs with three different PEG conformations did not significantly differ, whereas PEGylated micelles with the brush PEG conformation were rapidly cleared from the bloodstream. This indicates that the *in vivo* PK of PEGylated CCPs is primarily determined not by the PEG conformation but by the structural stability *in vivo*. Interestingly, the *in vivo* release kinetics of the model drug molecules included in the PEGylated CCPs depended on the PEG conformation and polarity of the model drug molecules. A hydrophilic molecule included in PEGylated CCPs with a mushroom PEG conformation in the shell exhibited relatively rapid clearance from the blood, which may be because this PEG conformation allowed water molecules to infiltrate the particle shell and promoted the molecular diffusion from the particle core to the water phase. In contrast, the water-swollen PEG shell of PEGylated CCPs inhibited the diffusion of hydrophobic molecules from the particle core, whereas PEGylated CCPs with a dense brush PEG conformation released the molecules more rapidly. However, the released molecules accumulated in tisses/organs at a high level, which may induce side effects of toxic anticancer drugs, whereas PEGylated CCPs did not accumulate. Our results suggest that future research on designing nanomedicines should focus on conferring structural stability and conjugating toxic drug molecules by chemical bonding to avoid side effects caused by undesired biodistribution.

■ ASSOCIATED CONTENT

Supporting Information

The Supporting Information is available free of charge at https://pubs.acs.org/doi/10.1021/acs.biomac.2c00730.

Synthesis procedure of PEGylated surfactants, NMR spectra, MALDI-TOF mass spectra, DLS data, SAXS profile of $\mathbf{P_xDU}$ micelles, SAXS fitting parameters, AF4 results for $\mathbf{P_xDU}$ micelles, summary of particle characteristics of $\mathbf{P_xDU}$ micelles, summary of physical parameters to determine PEG conformation, biodistribution of $\mathbf{P_xDU}$ micelles, summary of log *P* values, biodistribution of nCy5 and sCy5 included in **PEGx@CPs**, and summary of d*n*/d*c* values (PDF)

■ AUTHOR INFORMATION

Corresponding Author

Shota Fujii − *Department of Chemistry and Biochemistry, University of Kitakyushu, Kitakyushu, Fukuoka 808-0135, Japan*; orcid.org/0000-0002-6594-5211; Email: s-fujii@kitakyu-u.ac.jp

Authors

Takuma Kanamaru − *Department of Chemistry and Biochemistry, University of Kitakyushu, Kitakyushu, Fukuoka 808-0135, Japan*

Kazuo Sakurai − *Department of Chemistry and Biochemistry, University of Kitakyushu, Kitakyushu, Fukuoka 808-0135, Japan*; orcid.org/0000-0002-9737-0061

Complete contact information is available at: https://pubs.acs.org/10.1021/acs.biomac.2c00730

Author Contributions

The manuscript was written through the contribution of all authors. All authors have given approval to the final version of the manuscript.

Notes

The authors declare no competing financial interest.

■ ACKNOWLEDGMENTS

The authors acknowledge Dr Ji Ha Lee for the measurement of MALDI-TOF mass spectroscopy. All SAXS measurements were carried out at SPring-8 BL-40B2 (Proposal Nos. 2020A1228 and 2021B1215). This work was supported by JSPS KAKENHI: Grant-in-Aid for Scientific Research A (20H00668), Grant-in-Aid for Challenging Exploratory Research (20K20449), Grant-in-Aid for Scientific Research (19K15394), and Grant-in-Aid for Scientific Research B (22H01913).

■ ABBREVIATIONS

DLS, dynamic light scattering; ID, injected dose; MALS, multiangle light scattering; NMR, nuclear magnetic resonance; PS, polystyrene; RI, refractive index; SAXS, small-angle X-ray scattering

■ REFERENCES

(1) Cho, K.; Wang, X.; Nie, S.; Chen, Z.; Shin, D. M. Therapeutic Nanoparticles for Drug Delivery in Cancer. *Clin. Cancer Res.* **2008**, *14*, 1310−1316.

(2) Wilczewska, A. Z.; Niemirowicz, K.; Markiewicz, K. H.; Car, H. Nanoparticles as drug delivery systems. *Pharmacol. Rep.* **2012**, *64*, 1020−1037.

(3) Couvreur, P. Nanoparticles in drug delivery: Past, present and future. *Adv. Drug Delivery Rev.* **2013**, *65*, 21−23.

(4) Mitchell, M. J.; Billingsley, M. M.; Haley, R. M.; Wechsler, M. E.; Peppas, N. A.; Langer, R. Engineering precision nanoparticles for drug delivery. *Nat. Rev. Drug Discovery* **2021**, *20*, 101−124.

(5) Pelaz, B.; Alexiou, C.; Alvarez-Puebla, R. A.; Alves, F.; Andrews, A. M.; Ashraf, S.; Balogh, L. P.; Ballerini, L.; Bestetti, A.; Brendel, C.; et al. Diverse Applications of Nanomedicine. *ACS Nano* **2017**, *11*, 2313−2381.

(6) Pearce, A. K.; O'Reilly, R. K. Insights into Active Targeting of Nanoparticles in Drug Delivery: Advances in Clinical Studies and Design Considerations for Cancer Nanomedicine. *Bioconjugate Chem.* **2019**, *30*, 2300−2311.

(7) Rapoport, N. Physical stimuli-responsive polymeric micelles for anti-cancer drug delivery. *Prog. Polym. Sci.* **2007**, *32*, 962−990.

(8) Park, J. H.; Lee, S.; Kim, J.-H.; Park, K.; Kim, K.; Kwon, I. C. Polymeric nanomedicine for cancer therapy. *Prog. Polym. Sci.* **2008**, *33*, 113−137.

(9) Nyström, A. M.; Wooley, K. L. The Importance of Chemistry in Creating Well-Defined Nanoscopic Embedded Therapeutics: Devices Capable of the Dual Functions of Imaging and Therapy. *Acc. Chem. Res.* **2011**, *44*, 969−978.

(10) Elsabahy, M.; Wooley, K. L. Design of polymeric nanoparticles for biomedical delivery applications. *Chem. Soc. Rev.* **2012**, *41*, 2545−2561.
(11) Cabral, H.; Kataoka, K. Progress of drug-loaded polymeric micelles into clinical studies. *J. Controlled Release* **2014**, *190*, 465−476.
(12) Cabral, H.; Matsumoto, Y.; Mizuno, K.; Chen, Q.; Murakami, M.; Kimura, M.; Terada, Y.; Kano, M. R.; Miyazono, K.; Uesaka, M.; et al. Accumulation of sub-100 nm polymeric micelles in poorly permeable tumours depends on size. *Nat. Nanotechnol.* **2011**, *6*, 815−823.
(13) Poon, W.; Kingston, B. R.; Ouyang, B.; Ngo, W.; Chan, W. C. W. A framework for designing delivery systems. *Nat. Nanotechnol.* **2020**, *15*, 819−829.
(14) Pelegri-O'Day, E. M.; Lin, E.-W.; Maynard, H. D. Therapeutic Protein−Polymer Conjugates: Advancing Beyond PEGylation. *J. Am. Chem. Soc.* **2014**, *136*, 14323−14332.
(15) Chen, W.; Zhou, S.; Ge, L.; Wu, W.; Jiang, X. Translatable High Drug Loading Drug Delivery Systems Based on Biocompatible Polymer Nanocarriers. *Biomacromolecules* **2018**, *19*, 1732−1745.
(16) Maan, A. M. C.; Hofman, A. H.; de Vos, W. M.; Kamperman, M. Recent Developments and Practical Feasibility of Polymer-Based Antifouling Coatings. *Adv. Funct. Mater.* **2020**, *30*, No. 2000936.
(17) Chen, X.; Yang, D. Functional zwitterionic biomaterials for administration of insulin. *Biomater. Sci.* **2020**, *8*, 4906−4919.
(18) Takano, S.; Islam, W.; Nakazawa, K.; Maeda, H.; Sakurai, K.; Fujii, S. Phosphorylcholine-Grafted Molecular Bottlebrush−Doxorubicin Conjugates: High Structural Stability, Long Circulation in Blood, and Efficient Anticancer Activity. *Biomacromolecules* **2021**, *22*, 1186−1196.
(19) Otsuka, H.; Nagasaki, Y.; Kataoka, K. PEGylated nanoparticles for biological and pharmaceutical applications. *Adv. Drug Delivery Rev.* **2003**, *55*, 403−419.
(20) Walkey, C. D.; Olsen, J. B.; Guo, H.; Emili, A.; Chan, W. C. W. Nanoparticle Size and Surface Chemistry Determine Serum Protein Adsorption and Macrophage Uptake. *J. Am. Chem. Soc.* **2012**, *134*, 2139−2147.
(21) Blanco, E.; Shen, H.; Ferrari, M. Principles of nanoparticle design for overcoming biological barriers to drug delivery. *Nat. Biotechnol.* **2015**, *33*, 941−951.
(22) Suk, J. S.; Xu, Q.; Kim, N.; Hanes, J.; Ensign, L. M. PEGylation as a strategy for improving nanoparticle-based drug and gene delivery. *Adv. Drug Delivery Rev.* **2016**, *99*, 28−51.
(23) Alconcel, S. N. S.; Baas, A. S.; Maynard, H. D. FDA-approved poly(ethylene glycol)−protein conjugate drugs. *Polym. Chem.* **2011**, *2*, 1442−1448.
(24) Müllner, M.; Dodds, S. J.; Nguyen, T.-H.; Senyschyn, D.; Porter, C. J. H.; Boyd, B. J.; Caruso, F. Size and Rigidity of Cylindrical Polymer Brushes Dictate Long Circulating Properties In Vivo. *ACS Nano* **2015**, *9*, 1294−1304.
(25) Wang, Y.; Wang, D.; Jia, F.; Miller, A.; Tan, X.; Chen, P.; Zhang, L.; Lu, H.; Fang, Y.; Kang, X.; et al. Self-Assembled DNA−PEG Bottlebrushes Enhance Antisense Activity and Pharmacokinetics of Oligonucleotides. *ACS Appl. Mater. Interfaces* **2020**, *12*, 45830−45837.
(26) Xie, J.; Xu, C.; Kohler, N.; Hou, Y.; Sun, S. Controlled PEGylation of Monodisperse Fe3O4 Nanoparticles for Reduced Non-Specific Uptake by Macrophage Cells. *Adv. Mater.* **2007**, *19*, 3163−3166.
(27) Perry, J. L.; Reuter, K. G.; Kai, M. P.; Herlihy, K. P.; Jones, S. W.; Luft, J. C.; Napier, M.; Bear, J. E.; DeSimone, J. M. PEGylated PRINT Nanoparticles: The Impact of PEG Density on Protein Binding, Macrophage Association, Biodistribution, and Pharmacokinetics. *Nano Lett.* **2012**, *12*, 5304−5310.
(28) Cui, J.; De Rose, R.; Alt, K.; Alcantara, S.; Paterson, B. M.; Liang, K.; Hu, M.; Richardson, J. J.; Yan, Y.; Jeffery, C. M.; et al. Engineering Poly(ethylene glycol) Particles for Improved Biodistribution. *ACS Nano* **2015**, *9*, 1571−1580.
(29) Torchilin, V. P. Recent advances with liposomes as pharmaceutical carriers. *Nat. Rev. Drug Discovery* **2005**, *4*, 145−160.
(30) Klimek, L.; Novak, N.; Cabanillas, B.; Jutel, M.; Bousquet, J.; Akdis, C. A. Allergenic components of the mRNA-1273 vaccine for COVID-19: Possible involvement of polyethylene glycol and IgG-mediated complement activation. *Allergy* **2021**, *76*, 3307−3313.
(31) Sun, X.; Wang, G.; Zhang, H.; Hu, S.; Liu, X.; Tang, J.; Shen, Y. The Blood Clearance Kinetics and Pathway of Polymeric Micelles in Cancer Drug Delivery. *ACS Nano* **2018**, *12*, 6179−6192.
(32) Talelli, M.; Barz, M.; Rijcken, C. J. F.; Kiessling, F.; Hennink, W. E.; Lammers, T. Core-cross-linked polymeric micelles: Principles, preparation, biomedical applications and clinical translation. *Nano Today* **2015**, *10*, 93−117.
(33) Matsuno, J.; Kanamaru, T.; Arai, K.; Tanaka, R.; Lee, J. H.; Takahashi, R.; Sakurai, K.; Fujii, S. Synthesis and characterization of nanoemulsion-mediated core cross-linked nanoparticles, and in vivo pharmacokinetics depending on the structural characteristics. *J. Controlled Release* **2020**, *324*, 405−412.
(34) Yang, Q.; Jones, S. W.; Parker, C. L.; Zamboni, W. C.; Bear, J. E.; Lai, S. K. Evading Immune Cell Uptake and Clearance Requires PEG Grafting at Densities Substantially Exceeding the Minimum for Brush Conformation. *Mol. Pharm.* **2014**, *11*, 1250−1258.
(35) Du, X.-J.; Wang, J.-L.; Liu, W.-W.; Yang, J.-X.; Sun, C.-Y.; Sun, R.; Li, H.-J.; Shen, S.; Luo, Y.-L.; Ye, X.-D.; et al. Regulating the surface poly(ethylene glycol) density of polymeric nanoparticles and evaluating its role in drug delivery in vivo. *Biomaterials* **2015**, *69*, 1−11.
(36) Zhao, Z.; Ukidve, A.; Krishnan, V.; Mitragotri, S. Effect of physicochemical and surface properties on in vivo fate of drug nanocarriers. *Adv. Drug Delivery Rev.* **2019**, *143*, 3−21.
(37) Wu, B.; Zhang, L.-J.; Zhang, C.-J.; Deng, K.; Ao, Y.-W.; Mei, H.; Zhou, W.; Wang, C.-X.; Yu, H.; Huang, S.-W. Effect of Poly(ethylene glycol) (PEG) Surface Density on the Fate and Antitumor Efficacy of Redox-Sensitive Hybrid Nanoparticles. *ACS Biomater. Sci. Eng.* **2020**, *6*, 3975−3983.
(38) Cao, Z.-T.; Gan, L.-Q.; Jiang, W.; Wang, J.-L.; Zhang, H.-B.; Zhang, Y.; Wang, Y.; Yang, X.; Xiong, M.; Wang, J. Protein Binding Affinity of Polymeric Nanoparticles as a Direct Indicator of Their Pharmacokinetics. *ACS Nano* **2020**, *14*, 3563−3575.
(39) Hashimoto, T.; Tanaka, H.; Koizumi, S.; Naka, K.; Chujo, Y. A combined small-angle scattering study of a chemical reaction at specific sites and reaction-induced self-assembly as a problem in open non-equilibrium phenomena. *J. Appl. Crystallogr.* **2007**, *40*, s73−s77.
(40) Qhattal, H. S. S.; Hye, T.; Alali, A.; Liu, X. Hyaluronan Polymer Length, Grafting Density, and Surface Poly(ethylene glycol) Coating Influence in Vivo Circulation and Tumor Targeting of Hyaluronan-Grafted Liposomes. *ACS Nano* **2014**, *8*, 5423−5440.
(41) Zheng, P.; McCarthy, T. J. D4H/D4V Silicone: A Replica Material with Several Advantages for Nanoimprint Lithography and Capillary Force Lithography. *Langmuir* **2011**, *27*, 7976−7979.
(42) Feigin, L. A.; Svergun, D. I. *Structure Analysis by Small-Angle Xray and Neutron Scattering*; Plenum Press: New York, 1987.
(43) Tanaka, R.; Arai, K.; Matsuno, J.; Soejima, M.; Lee, J. H.; Takahashi, R.; Sakurai, K.; Fujii, S. Furry nanoparticles: synthesis and characterization of nanoemulsion-mediated core cross-linked nanoparticles and their robust stability in vivo. *Polym. Chem.* **2020**, *11*, 4408−4416.
(44) Pedersen, J. S.; Gerstenberg, M. C. Scattering Form Factor of Block Copolymer Micelles. *Macromolecules* **1996**, *29*, 1363−1365.
(45) Israelachvili, J. N. *Intermolecular and Surface Forces*; Academic press: London, 1992; Vol. *450*.
(46) Ouyang, B.; Poon, W.; Zhang, Y.-N.; Lin, Z. P.; Kingston, B. R.; Tavares, A. J.; Zhang, Y.; Chen, J.; Valic, M. S.; Syed, A. M.; et al. The dose threshold for nanoparticle tumour delivery. *Nat. Mater.* **2020**, *19*, 1362−1371.
(47) Molinspiration Pr operty Calculation Service. http://www.molinspiration.com/services/volume.html (accessed Jan 15, 2022).
(48) Binauld, S.; Stenzel, M. H. Acid-degradable polymers for drug delivery: a decade of innovation. *Chem. Commun.* **2013**, *49*, 2082−2102.

https://doi.org/10.1021/acs.biomac.2c00730
Biomacromolecules 2022, 23, 3909−3918

(49) Zhang, R.; Nie, T.; Fang, Y.; Huang, H.; Wu, J. Poly(disulfide)-s: From Synthesis to Drug Delivery. *Biomacromolecules* **2022**, *23*, 1−19.

https://doi.org/10.1021/acs.biomac.2c00730
Biomacromolecules 2022, 23, 3909−3918